Review Article

Raman Spectroscopy in Graphene-Based Systems: Prototypes for Nanoscience and Nanometrology

Ado Jorio

Departamento de Física, Universidade Federal de Minas Gerais, 30123-970 Belo Horizonte, MG, Brazil

Correspondence should be addressed to Ado Jorio, adojorio@fisica.ufmg.br

Raman spectroscopy is a powerful tool to characterize the different types of sp^2 carbon nanostructures, including two-dimensional graphene, one-dimensional nanotubes, and the effect of disorder in their structures. This work discusses why sp^2 nanocarbons can be considered as prototype materials for the development of nanoscience and nanometrology. The sp^2 nanocarbon structures are quickly introduced, followed by a discussion on how this field evolved in the past decades. In sequence, their rather rich Raman spectra composed of many peaks induced by single- and multiple-resonance effects are introduced. The properties of the main Raman peaks are then described, including their dependence on both materials structure and external factors, like temperature, pressure, doping, and environmental effects. Recent applications that are pushing the technique limits, such as multitechnique approach and *in situ* nanomanipulation, are highlighted, ending with some challenges for new developments in this field.

1. Introduction

Raman spectroscopy is the inelastic scattering of light by matter, from molecules to crystals [1]. The effect is highly sensitive to the physical and chemical properties of the scattering material, as well as to any environmental effect that may change these properties. For this reason, the Raman spectroscopy is evolving into one of the most useful tools for the development of nanoscience and nanometrology. Raman spectrometers are widely available; the technique is relatively simple to perform, possible to carry out at room temperature and under ambient pressure, and requiring relatively simple or no specific sample preparation. Optical techniques (if not using high-energy photons) are nondestructive and non-invasive, as they use a massless and chargeless particle, the photon, as a probe, which is especially important for nanoscience due to the large surface-to-volume ratio in nano-materials.

Two-dimensional graphene, one-dimensional carbon nanotubes, and the related disordered materials, here all referred to as sp^2 nanocarbons, are selected as the prototype materials to be discussed, first due to their importance to nanoscience and nanotechnology, second because their Raman spectra have been extremely useful in advancing our knowledge about these nanostructures.

Nature shows that it is possible to manipulate matter and energy by assembling complex self-replicating carbon-based structures that are able to sustain life. On the other hand, carbon is the upstairs neighbor to silicon in the periodic table, with carbon having more flexible bonding and having unique physical, chemical, and biological properties, holding promise for a revolution in electronics at some future time. Three important factors make sp^2 nanocarbons special.

(1) The unusually strong covalent σ bonding between neighboring carbon atoms. This strength is advantageous for sp^2 nanocarbons as a prototype material for the development of nanoscience and nanotechnology, since different interesting nanostructures (sheets, ribbons, tubes, horns, cages, etc.) are stable and strong enough for exposure to many different types of characterization and processing steps.

(2) The sp^2 nanocarbons, which include graphene and carbon nanotubes, fullerenes, and other carbonaceous materials, are also called π electron materials

due to the extended π electron clouds. The delocalized electronic states in monolayer graphene are highly unusual, because they behave like relativistic Dirac Fermions, that is, these states exhibit a massless-like linear energy momentum relation, and are responsible for unique transport (both thermal and electronic) properties at sufficiently small energy and momentum values. This unusual electronic structure is also responsible for unique optical phenomena.

(3) The simplicity of the sp^2 nanocarbon systems, which are systems formed by only one type of atom in a periodic hexagonal structure. Therefore, different from most materials, sp^2 nanocarbons allow us to easily access their special properties using both experimental and theoretical approaches, enabling us to model the structure for the development of our methodologies and knowledge.

Finally, it is very advantageous that with a common Raman spectroscopy apparatus, one can observe the Raman scattering response from one single graphene sheet, as well as from one isolated single-wall carbon nanotube (SWNT). The similarities and differences in the Raman spectra for the different sp^2 nanocarbons pave the route for understanding the potential of Raman spectroscopy in nanoscience and nanometrology [2].

This paper is organized as follows: Section 2 quickly introduces the atomic structure of the sp^2 nanocarbons. Section 3 describes the historical development of Raman spectroscopy applied to sp^2 nanocarbons. Section 4 discusses the general aspect of the sp^2 nanocarbons Raman spectra, related to both first and higher-order scattering events, mostly induced by resonance effects. The momentum-selective resonance mechanisms in the sp^2 nanocarbon Raman spectroscopy are discussed in Section 5. Section 6 describes the detailed behavior of the most intense features, named D, G, G′, and RBM bands. Section 7 describes the new achievements that are pushing the limits of Raman spectroscopy on sp^2 nanocarbons, such as multitechnique approach and *in situ* nanomanipulation, including also the applications to cross-related fields like biotechnology and soil science. Section 8 closes the paper with conclusions and pointing some challenges for further developments.

2. The sp^2 Nanocarbons Structure

The fundamental crystal that constitutes the basis of sp^2 nanocarbons is graphene, a two-dimensional (2D) planar structure composed by packing hexagons (see Figure 1, left). The carbon atoms are located at the vertices of the hexagons, and a two C atoms unit cell can be used to reproduce the entire structure by applying the appropriated translation operations. When many graphene layers are put on top of each other, the resulting material is graphite.

By cutting a graphene layer, a graphene nanoribbon can be constructed. By rolling such a ribbon into a cylinder, one generates a carbon nanotube (see Figure 1, right). The carbon nanotube can be achiral, like the one shown in
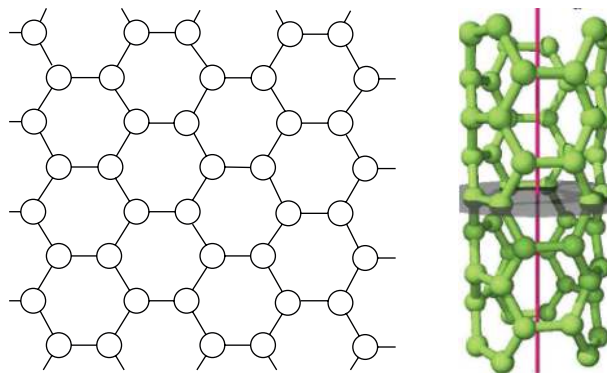

FIGURE 1: Schematic structure of graphene (left) and a achiral single-wall carbon nanotube (right). Each circle in the graphene and sphere in the nanotube represents a carbon atom. Each carbon atom is bonded to three carbon neighbours by covalent bonds. The grey plane crossing the nanotube represents a mirror symmetry which occurs in the achiral tubes [2].

Figure 1, or chiral (not shown), where the carbon bonds exhibit a helical structure around the SWNT axis direction.

Other sp^2 nanocarbons, like fullerenes, nanocones, and nanohorns, require the introduction of defects in the hexagonal structure to break the planar structure. The most common is the replacement of a hexagon by a pentagon. A fullerene is composed of 12 hexagons to fully close the structure in a "football-like" cage structure ("soccer-like" for North Americans). The number of hexagons can start from zero and increase indefinitely, making larger and larger carbon cages. The football-like structure is composed by a total of 60 atoms, thus being named the C_{60}. Strictly speaking, the C–C bonds in such structures have a mixing of the σ and π bonds, the degree of mixing depending on the degree of planar deformation.

3. Historical Development of Raman Spectroscopy Applied to sp^2 Nanocarbons

Raman spectroscopy has been used to study carbon structures since its discovery [1]. However, when applied to sp^2 nanocarbons, there is a milestone in the early seventies, in the field of nanographite and amorphous carbons [3], followed by many important works in that decade (e.g., [4, 5]). The technique has encountered important applications in the field of ion implantation and graphite intercalation compounds [6], and its success on this field kept increasing with applications to fullerenes [7], carbon nanotubes [8], and finally the mother material graphene [9]. While the main route of the solid-state physics approach has provided the framework for the great majority of the studies in this field, quantum chemical studies of polyaromatic compounds were crucial for understanding different uncommon aspects related to the Raman spectra of sp^2 nanocarbons [10].

Important developments in our understanding of the Raman spectroscopy applied to graphene-based systems happened in the early 21st century. In 2000, Ferrari and Robertson [11] described qualitatively the amorphization

trajectory from graphite to tetrahedral amorphous carbon. They proposed a three-stage classification of disorder: stage 1, from graphite to nanocrystalline graphite; stage 2, from nanocrystalline graphite to low sp^3 amorphous carbon; stage 3, from low to high sp^3 (tetrahedral) amorphous carbon.

In the same year, Thomsen and Reich [12] introduced the double-resonance mechanism to explain the observation and dispersive behaviour of the disorder-induced D band in defective graphite, appearing near $1350\,cm^{-1}$ for excitation with a 514 nm wavelength laser. This solid-state physics approach was shown to be consistent with quantum chemical studies of polyaromatic compounds to explain the D band [10]. While the two approaches are complementary to understand the phenomena, the solid-state physics approach can be made analytical, allowing further advances. For example, Saito et al. [13] extended the double-resonance model, including intravalley and intervalley electron-phonon scattering mechanisms and application to all phonon branches in different sp^2 carbons.

Still in 2000, Rao et al. [14] were the first to explore one-dimensional selection rules in the Raman spectra of multiwall carbon nanotubes (MWNTs), and this study was further clarified performing experiments on SWNTs and using group theory [15–17].

A breakthrough in the field came with the launch of single-nanotube spectroscopy in 2001 [18], showing that carbon nanotubes could be studied at the isolated tube level. Each SWNT species was shown to present specificities in the Raman scattering processes, thus starting the single-nanotube spectroscopy rush. Realization of single graphene nanoribbon spectroscopy came a few years later [19].

Based on the double-resonance mechanics, in 2002, Souza Filho et al. [20] demonstrated how the second-order Raman spectra could be used to provide information about changes in the electronic structure of different (n, m) SWNTs. A few years later, in 2006, Ferrari et al. [21] used the same concept to show that Raman spectroscopy could be applied as a very simple and straightforward method to determine the number of layers in a graphene sample. Similar results were obtained simultaneously by Gupta et al. [22].

In 2003, two different groups, Hartschuh et al. [23] and Hayazawa et al. [24], observed, for the first time, the tip-enhanced Raman spectroscopy (TERS) from carbon nanotubes. Due to their low dimensionality and huge optical response, carbons nanotubes started to be widely used as a prototype for the development of TERS. Some results achieved in carbon nanotubes were nanoscale vibrational analysis [25], nanoscale optical imaging of excitons [26], TERS polarization measurements [27], imaging of nanotube chirality changes [28], spectral determination of single-charged defects [29], and local optical response of semiconducting nanotubes to DNA wrapping [30], among others. A comprehensible review for TERS in carbon nanotubes can be found in [31]. In the case of graphene, a few results are appearing in the literature [32–35], including the imaging of defects and contaminants [36].

In 2004, Cançado et al. [37] showed that the disorder-induced D band intensity in graphite edges depends on the edge atomic structure, differentiating the zigzag from the armchair edge. A few years later, in 2009, Casiraghi et al. [38] showed that the same effect could be observed in graphene. In the same year, the quantum chemical calculations approach was shown to be consistent with the solid-state physics predictions for the zigzag versus armchair edge response [39].

High-level doping effects could also be assessed in carbon nanotubes, as summarized in 2003 for chemical doping by Filho et al. [40], and in 2004 for electrochemical doping by Corio et al. [41]. As demonstrated later, understanding low-doping effects had to wait for the introduction of new concepts.

The different Raman scattering phenomena—1st and multiple-order, single, and multiple resonances—responsible for the Raman features were established, but quantitative accurate description of the main features was restricted to empirical models [42, 43]. Despite so many studies, the phonon dispersion for the optical modes near the high-symmetry Γ and K points was not accurately described theoretically, leading to the development of different and unsuccessful models. A very important conceptual change was then proposed by Piscanec et al. [44] in 2004, with the introduction of the Kohn anomaly physics in the graphite phonon dispersion. This new concept was applied successfully to describe the phonon dispersion of graphite near the high-symmetry points in the Brillouin zone and to understand and characterize low doping levels in both graphene [45] and carbon nanotubes [46, 47]. The Raman frequencies, including their dependence on strain and doping, were understood [48, 49], and the overall consistency with quantum chemistry calculations was established [50].

Starting from 2004, resonance Raman spectroscopy with many excitation laser lines was extensively applied for the determination of the optical transitions (E_{ii}) in SWNTs by Fantini et al. [51], Telg et al. [52], Araujo et al. [53], and Doorn et al. [54], among others, and in double-wall carbon nanotubes (DWNTs) by Pfeiffer et al. [55]. All this development came together with the introduction of many-body physics (electron-electron and electron-hole interactions) for accurate description of E_{ii} and the Raman matrix elements in SWNTs, by Jiang et al. [56, 57].

Finally, the introduction of environmental effects in both vibrational [58] and electronic properties [59] of SWNTs was largely studied, staring in 2008 by Araujo et al. [58, 59]. The effect of the dielectric constant in SWNTs was shown to depend on the SWNT diameter due to the presence of electric field inside the *quasi*-one-dimensional tube [59, 60].

4. General Aspect of the sp^2 Nanocarbons Raman Spectra

Different aspects have to be considered to understand why the Raman spectroscopy has played a very important role in the development of the science related to sp^2 nanocarbons: (1) vibrations in carbon nanostructures strongly modulate the Raman polarizability tensor, and the scattering processes are resonant because of the π electrons, guaranteeing a strong response; (2) the Raman spectra exhibit peaks with relatively

high frequencies ω because of the high stiffness of the C–C bonds, and any small frequency change (less than 1%) is easily detectable with broadly available spectrometers; (3) the resonance effects make it possible to study both phonons and electrons, and multiple resonances enhance special scattering processes probing phonons in the interior of the Brillouin zone.

The Raman spectra from sp^2 nanocarbons are composed of many peaks coming from first-order and higher-order scattering processes (see Figure 2). The Raman features can all be related to phonons in graphene, not only at the Brillouin zone center, but also from the interior of the Brillouin zone. The modes associated with interior points are activated either by higher-order (combination modes and overtones) processes or by defects which break the $q = 0$ momentum selection rule [2, 12] (see Section 5). The modes from the interior of the Brillouin zone can be dispersive (frequency changes with changing the excitation laser energy E_{laser}), and therefore, they can be used for measuring the electron and phonon dispersion based on the double-resonance model. However, according to the multiple-resonance model, the Raman features are composed of averages of phonons around the high-symmetry points and lose well-defined momentum information. Table 1 provides a summary of the assignments of many of these features in the Raman spectra [2]. The results give average values that usually exhibit small deviations depending on the sp^2 nanocarbon structure and on the ambient conditions.

5. Momentum-Selective Resonance Mechanisms in sp^2 Nanocarbon Raman Spectroscopy

As pointed in Section 4, the scattering processes are resonant because of the π electrons. In a perfectly crystalline structure, translational symmetry guarantees momentum conservation, so that only Γ point phonons ($q = 0$) can be Raman active in a one-phonon (first-order) scattering process. In grapheme-related systems, this resonance process gives rise to the G band peak, and the respective resonance process is displayed in Figure 3. The red circle in the graphene phonon dispersion (left part of Figure 3) shows the G band momentum and frequency. On the right part of Figure 3, the G band eigenvector is shown (top), as well as the electronic transitions induced by the incoming photon (green), by the G band phonon (black) and generating the outgoing photon (red). The Γ point phonon near $870\,cm^{-1}$ is not Raman active, but it can be seen by infrared absorption experiments.

When higher-order scattering events are considered, for example, two-phonon scattering with $+q$ and $-q$ momentum transfer, or when defects in the lattice break the crystal translational symmetry, phonons with $q \neq 0$ momentum are Raman allowed [12, 13]. In these cases, specific phonons will be selected in the sp^2 nanocarbons Raman spectra, due to higher-order resonance effects, as displayed in Figure 4. Both electron-photon (upwards green arrow) and electron-phonon (diagonal black solid arrows) scattering processes are resonant. After the electronic transition induced by absorbing the incoming photon (green vertical arrow), the electron in the valence band can be scattered by a $q \neq 0$ momentum phonon resonantly, considering that the phonon energy and momentum will connect two real electronic states, as indicated by the black diagonal solid arrows indicated by D and D′ in Figure 4. The diagonal black-dashed arrow indicates a nonresonant scattering. These special D and D′ phonons can be mapped back into the graphene phonon dispersion, and they lye either near the Γ (intra-valley scattering) or near the K (inter-valley scattering) point in the Brillouin zone (see Figure 4, top right). For the D band phonon, there are two optical branches close in energy, the in-plane transversal optical (iTO) and the in-plane longitudinal optical (iLO). The D band, as well as the second-order G′ (or 2D) band, comes from the TO mode (red branch in Figure 3) because the electron-phonon coupling near K is much stronger for the TO phonon than for the LO phonon. However, as described in Section 4, all phonon branches can generate the multiple-resonance Raman scattering processes, thus generating a large number of peaks in the Raman spectra from sp^2 nanocarbons [13], as shown in Figure 2. Most of these peaks exhibit relatively low intensity due to the weak electron-phonon coupling.

6. Detailed Behaviour of the Main Features

Although the Raman spectra of graphitic materials consist of a large number of peaks, as discussed in the previous sections, most of them are relatively weak. The most intense peaks and broadly used to study and characterize these materials are the G and D bands, appearing around $1585\,cm^{-1}$ and $1350\,cm^{-1}$, respectively. The G peak corresponds to the first-order Raman-allowed E_{2g} phonon at the Brillouin zone centre (see eigenvector schematics in Figure 3—top-right). The D peak is related to the breathing modes of the six-atom rings (see K point eigenvector schematics in Figure 4—bottom-right) and requires a defect for its activation. The G′ peak, related to the second order of the D peak, is also strong and important for sp^2 nanocarbon characterization. Finally, the radial breathing mode (RBM), present only in SWNTs, is the key feature for SWNT studies. The characteristics for these most intense Raman features are presented in Figure 5 for different sp^2 nanocarbons, and a summary of how they are used to characterize sp^2 nanocarbons is discussed here.

6.1. The G Band. The G band, related to the C–C bond stretching (see eigenvector in Figure 3), is the main Raman signature for all sp^2 carbons, and it is observed as a peak (or a multipeak feature) at around $1585\,cm^{-1}$ (see Figure 5). The G band properties can be summarized as follows.

(i) Hydrostatic pressure on graphene shifts its frequency ω_G.

(ii) Uniaxial stretching of graphene splits the G peak into G^- and G^+, which are, respectively, related to atomic motion along and perpendicular to the stretching direction. Increasing the stretching redshifts both ω_{G^+} and ω_{G^-}.

(iii) Doping graphene blueshifts ω_G for weak doping (changes in the Fermi level near the K point). Higher
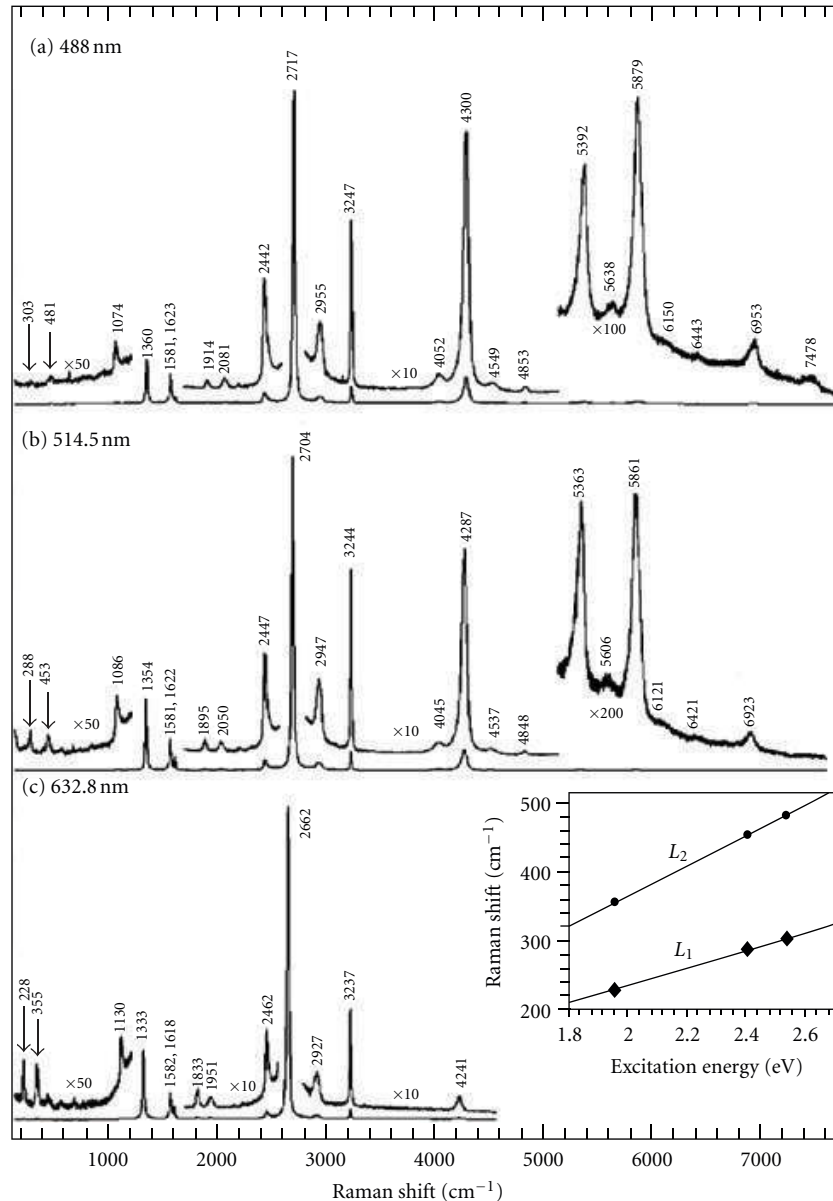
FIGURE 2: One of the most beautiful Raman spectra of sp^2 nanocarbons found in the literature. They come from graphite whiskers obtained at three different laser wavelengths (excitation energies), as measured by Tan et al. [61]. Note that some phonon frequencies vary with E_{laser} and some do not. Above 1650 cm^{-1}, the observed Raman features are all multiple-order combination modes and overtones, though some of the peaks observed below 1650 cm^{-1} are actually one phonon-bands activated by defects. The inset to (c) shows details of the peaks labeled by L_1 and L_2, involving the acoustic iTA and LA branches, respectively, according to the double-resonance Raman scattering model.

doping levels can cause blue (red) shift for p (n) doping.

(iv) Increasing temperature (T) generally redshifts ω_G. Different effects take place, such as changes in the electron-phonon renormalization, phonon-phonon coupling, and ω_G shifts due to thermal expansion-induced volume changes.

(v) When choosing light polarized in the graphene plane (propagation perpendicular to the sheet), then rotating the polarization is irrelevant for unstrained or homogeneously strained graphene. If graphene is inhomogeneously strained, then the relative intensity between the G$^+$ and G$^-$ peaks I$_G{}^+$/I$_G{}^-$ will give the strain direction.

(vi) The linewidth for the G peak is usually in the range of 10–15 cm^{-1}, although it changes with strain, temperature, and doping.

(vii) Bending the graphene sheet splits the G band into ω_{G^+} and ω_{G^-}, which have their atomic vibrations preferentially along and perpendicular to the folding axis, respectively.

TABLE 1: Assignments and frequency behavior for the Raman modes from sp^2 carbon materials [2].

Name[1]	ω (cm^{-1})[2]	Res.[3]	$\partial\omega/\partial E$[4]	Notes[5]
iTA	288	DRd1	129	Intra-V ($q \sim 2k$ near Γ)
LA	453	DRd1	216	Intra-V ($q \sim 2k$ near Γ)
RBM[6]	$227/d_t$	SR	0	SWNT vibration of radius
IFM$^-$ (oTO − LA)	750	DR2	−220	Intra-V + Intra-V ($q \sim 2k$ near Γ)
oTO	860	DRd1	0	Intra-V ($q \sim 0$ near Γ), IR active
IFM$^+$ (oTO + LA)	960	DR2	180	Intra-V + Intra-V ($q \sim 2k$ near Γ)
D (iTO)	1350	DRd1	53	Inter-V ($q \sim 2k$ near K)
G (iTO·LO)[7]	1585	SR	0	$q = 0$, that is, at Γ
D′ (LO)	1620	DRd1	10	Intra-V ($q \sim 2k$ near Γ)
M$^-$ (2oTO)	1732	DR2	−26	Intra-V + Intra-V ($q \sim 2k$ near Γ)
M$^+$ (2oTO)	1755	DR2	0	Intra-V + Intra-V ($q \sim 0$ near Γ)
iTOLA (iTO + LA)	1950	DR2	230	Intra-V + Intra-V ($q \sim 2k$ near Γ)
G* (LA + iTO)	2450	DR2	−10	Inter-V + Inter-V ($q \sim 2k$ near K)[8]
G′ (2iTO)[9]	2700	DR2	100	Inter-V + Inter-V ($q \sim 2k$ near K)
G + D	2935	DRd2	50	Intra-V + Inter-V[10]
D′ + D	2970	DRd2	60	Intra-V + Inter-V[10]
2G	3170	DR2	0	Overtone of G mode
2D′	3240	DR2	20	Overtone of D′ mode

[1] Usually the respective graphene phonon branch labels the Raman peaks. When other names are given in the literature, the respective phonon branch appears between parentheses.
[2] The frequencies quoted in the table are observed at E_{laser} = 2.41 eV.
[3] The notation for resonances is as follows: SR: single resonance, 1-phonon Raman allowed; DR2: double resonance, 2-phonon Raman allowed; DRd1: double resonance Raman activated by disorder, 1 phonon; DRd2: double resonance Raman activated by disorder, 2 phonons.
[4] The change of phonon frequency in cm^{-1} obtained by changing the laser excitation energy by 1 eV.
[5] Intra-V: intravalley scattering; Inter-V: intervalley scattering.
[6] The radial breathing mode (RBM) only occurs for carbon nanotubes.
[7] The iTO and LO phonons are degenerated at the Γ point for graphene. For nanoribbons and SWNTs, the G band splits into several peaks due to symmetry, and differs for metallic and semiconducting nanotubes. The G band frequency depends strongly on doping and strain.
[8] There is another assignment of 2iTO ($q \sim 0$ near K) with $\partial\omega/\partial E \sim 0$.
[9] Some groups use the nomenclature "2D band" for the G′ band.
[10] This combination mode consists of intra-valley + inter-valley scattering, and thus, the elastic scattering process also exists for some combination modes.

(viii) Rolling up the graphene sheet into a seamless tube (SWNT) causes the following effects: (1) bending splits the G band into ω_{G^+} and ω_{G^-}, which are preferentially along (LO) and perpendicular (TO) to the tube (folding) axis, respectively, for semiconducting SWNTs. For metallic tubes, electron-phonon coupling softens the LO modes, so that ω_{G^+} and ω_{G^-} are actually associated with TO and LO, respectively. (2) Quantum confinement generates up to 6 Raman-allowed G band peaks, three of each exhibiting LO- or TO-like vibrations, two totally symmetric A1 modes, two E1 modes, and two E2 symmetry modes. Due to the depolarization effect and special resonance conditions, the A1 modes usually dominate the G band spectra.

(ix) Decreasing the SWNT diameter increases the bending and shifts mostly ω_{G^-}. The ω_{G^-} shift can be used to measure the SWNT diameter.

(x) Changing the SWNT chiral angle θ changes the intensity ratio between LO- and TO-like modes.

(xi) Hydrostatic pressure on SWNT bundles shifts ω_G.

(xii) Strain on isolated SWNTs under hydrostatic and uniaxial deformation, torsion, bending, and so forth, changes G$^-$ and G$^+$, depending on the tube structure, as defined by the chiral indices (n, m).

(xiii) Doping SWNTs changes ω_G, mainly for metallic SWNTs. There is a rich doping dependence on (n, m), but a strong effect is felt mostly on the broad and downshifted G$^-$ peak in metallic SWNTs, with doping usually causing an upshift and sharpening of the G$^-$ feature.

(xiv) Temperature change generates similar effects in SWNTs and graphene. Increasing T softens and broadens the G band peaks in SWNTs.

(xv) Polarization analysis in SWNTs can be used to assign the G band mode symmetries.

6.2. The G′ Band. The G′ band is the second-order sp^2 Raman signature, observed for all sp^2 carbons as a peak (or a multipeak feature) in the range of 2500–2800 cm^{-1} (see Figure 5), changing with E_{laser}. The G′ band properties can be summarized as follows.
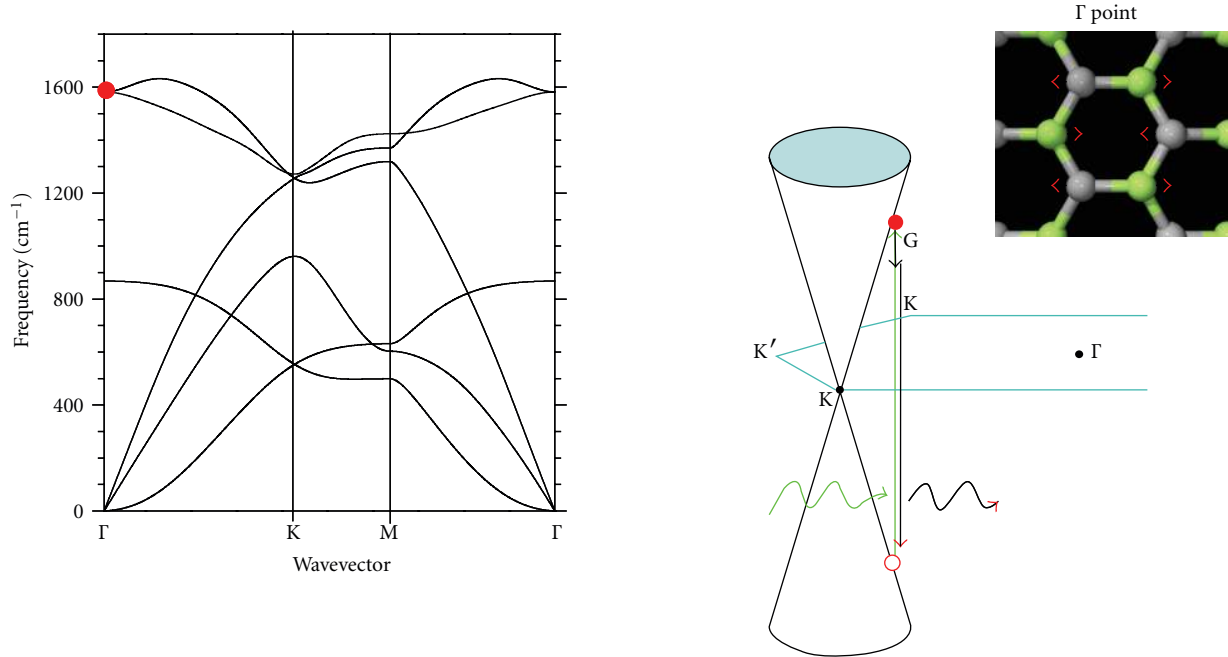
FIGURE 3: Resonance process for the G band. On the left, the graphene phonon dispersion is shown, with a red-filled circle indicating the G band frequency and momentum. On the top right, the G band eigenvector is shown by the red arrows. On the bottom right, a zoom near the K point electronic dispersion shows the cone structure for the π bands near the Fermi level (the Dirac cone). The wavy arrows indicate the incoming (green) and outgoing (red) photons. The electronic transitions induced by the incoming photon (green), the G band phonon (black), and the outgoing photon (red) are indicated by the vertical arrows.

(i) The G$'$ frequency $\omega_{G'}$ appears at 2700 cm^{-1} for E_{laser} = 2.41 eV, but its frequency changes by changing E_{laser}. Its dispersion is $(\partial\omega_{G'}/\partial E_{laser}) \simeq 90$ cm^{-1}/eV for monolayer graphene, and this dispersion changes slightly by changing the sp^2 nanocarbon structure. The sensitivity of $\omega_{G'}$ to the detailed sp^2 structure makes this band a powerful tool for quantifying the number of graphene layers and the stacking order in few-layer graphenes and graphite, and for characterizing SWNTs by the diameter and chiral angle dependence of $\omega_{G'}$ and the G$'$ band intensity.

(ii) The G$'$ band depends on the number of graphene layers: one-layer graphene (1LG) exhibits a single Lorentzian peak in the G$'$ band, and the intensity of the G$'$ band is larger (24 times) than that of the G band in 1LG. In contrast, 2LG with AB Bernal stacking exhibits four Lorentzian peaks in the G$'$ band, and the intensity of the G$'$ band with respect to the G band is strongly reduced (same magnitude or smaller). For 3LG with AB Bernal stacking, 15 scattering processes are possible for the G$'$ band, but the 15 peaks occur close in frequency and cannot all be distinguished from each other. Usually the G$'$ band from 3LG is fitted with 6 peaks. Highly oriented pyrolytic graphite (HOPG) exhibits two G$'$ peaks. Turbostratic graphite exhibits only a single G$'$ peak, and care should be taken when assigning the number of layers based on the G$'$ feature. The single G$'$ peak in turbostratic graphite is slightly blueshifted ($\sim$8 cm^{-1}) from the G$'$ peak in 1LG.

(iii) While HOPG (considered as a three-dimensional structure) exhibits a two-peak G$'$ feature, turbostratic graphite (no AB Bernal stacking order and considered as a two-dimensional structure) exhibits a single Lorentzian line. Therefore, the single- versus double-peak G$'$ structure can be used to assign the amount of stacking order present in actual graphite samples.

(iv) By changing E_{laser}, it is possible to probe different electrons and phonons in the interior of the Brillouin zone, according to the double-resonance model. The G$'$ band probes the iTO phonons near the K point, where the strongest electron-phonon coupling occurs.

(v) The G$'$ feature can be used to assign p and n type doping in graphene and SWNTs. A blueshift (redshift) is observed for p (n) doping. The magnitude of the shift depends also on the specific type of doping atom, while the relative intensity between doped and undoped pristine G$'$ band peaks can be used to obtain the dopant concentration.

(vi) Carbon nanotubes show a very special G$'$ band feature, where the number of peaks and their frequencies depend on (n, m) due to both curvature-induced strain and the quantum confinement of their electronic and vibrational structures. The resonance
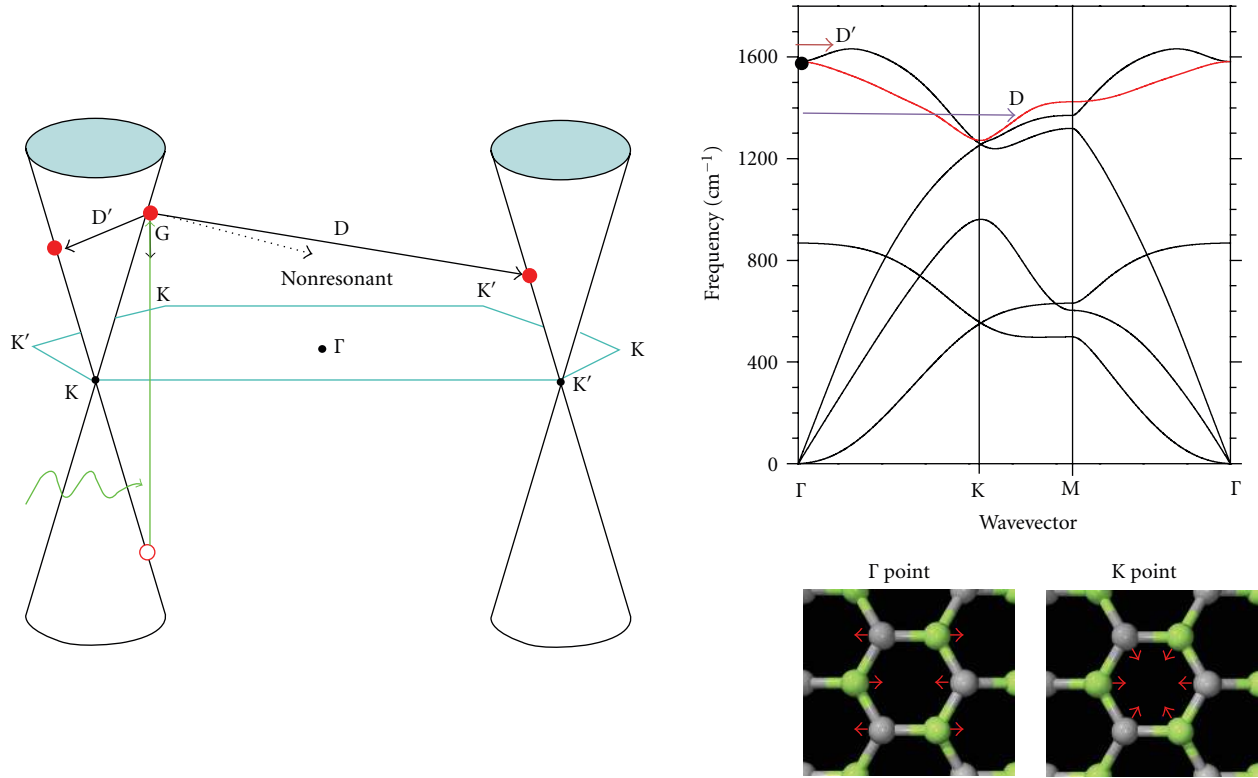
FIGURE 4: Multiple-resonance processes for the D and D′ bands. On the left, the first Brillouin zone showing two electronic Dirac cones for the π electron dispersion in the nonequivalent K and K′ points. The green wavy arrow indicates the incoming photon. The electronic transition induced by the incoming light is indicated by the green upwards arrow. The phonon-induced transitions are indicated by black arrows: the G band phonon (vertical downwards), the D and D′ band phonons (diagonal black solid arrows) and a nonresonant process (diagonal black dashed arrow). On the top right, the graphene phonon dispersion with the D and D′ band energy and momentum indicated by the vertical arrows. On the bottom right, the optical phonon eigenvectors for the high-symmetry Γ and K points.
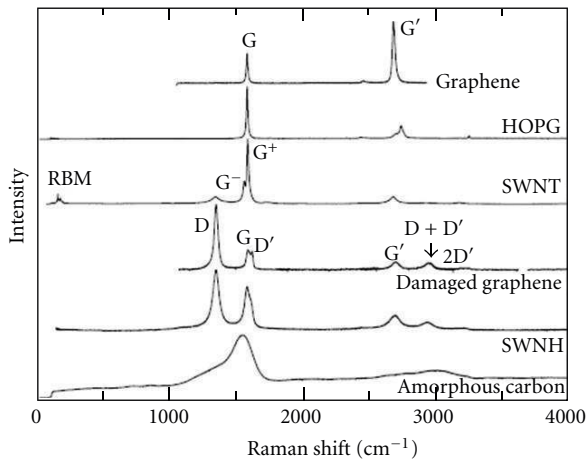

FIGURE 5: Raman spectra from several sp^2 nanocarbons. From top to bottom: crystalline monolayer graphene, highly oriented pyrolytic graphite (HOPG), single-wall carbon nanotubes (SWNT) bundle sample (notice the presence of the RBMs at low frequencies), damaged graphene (notice the appearance of disorder-induced peaks), single wall carbon nanohorns (SWNHs), and hydrogenated amorphous carbon. Some Raman peaks are labeled in a few of the spectra [2].

condition is restricted to $E_{laser} \approx E_{ii}$ and $E_{laser} \approx E_{ii} + E_{G'}$, and this fact gives rise to a $\omega_{G'}$ dependence on the SWNT diameter and chiral angle.

6.3. The D Band. The D band is the dominant sp^2 Raman signature of disorder (or defects). It is observed as a peak in the range of 1250–1400 cm^{-1} (see Figure 5), and it is related to the breathing of the carbon hexagons (see eigenvector in Figure 4). The D band properties can be summarized as follows.

(i) The D band frequency ω_D appears at 1350 cm^{-1} for $E_{laser} = 2.41$ eV, but its frequency changes by changing E_{laser}. Its dispersion is $(\partial\omega_{D'}/\partial E_{laser}) \simeq 50$ cm^{-1}/eV for monolayer graphene, and it changes slightly by changing the sp^2 nanocarbon structure. For SWNTs, the frequency ω_D depends on the nanotube diameter as well.

(ii) The D band intensity can be used to quantify disorder. The effect of nanocrystallite size and Ar$^+$ bombardment dose has been used to characterize the disorder in both SWNTs and graphene, and a phenomenological model has been developed for

explaining the D band intensity evolution with the amount of disorder.

(iii) Being disorder related, the D band linewidth can change from 7 cm^{-1} (observed for isolated SWNTs) to a hundred wavenumbers (for very defective carbon materials).

(iv) The D band scattering is forbidden at edges with zigzag structure. This property can be used to analyze the edge structure and to distinguish zigzag from armchair edges.

(v) Because absolute intensity measurement is a difficult task in Raman spectroscopy, the normalized intensity I_D/I_G ratio is largely used to measure the amount of disorder. This ratio depends not only on the amount of disorder, but also on the excitation laser energy, since $I_G \propto E_{laser}^4$, while I_D is E_{laser} independent (when measured in the 1.9–2.7 eV range).

(vi) Since the D band is activated by defects, it can only be observed near the defect within a coherence length ℓ. The D band was used to obtain $\ell = 2$ nm for ion-bombarded graphene measured with $E_{laser} = 2.41$ eV.

6.4. The Radial Breathing Mode (RBM). The radial breathing mode (RBM) is the Raman signature for the presence of carbon nanotubes, related to the "tube-breathing-like" motion. The RBM is observed as a peak (or a multipeak feature) in the 50–760 cm^{-1} range (see Figure 5). The RBM properties can be summarized as follows.

(i) The ω_{RBM} depends on diameter (d_t), according to $\omega_{RBM} = (227/d_t) * \sqrt{(1 + C_e * d_t^2)}$, where C_e (nm^{-2}) probes the effect of the environment on ω_{RBM}.

(ii) The ω_{RBM} is predicted to depend on SWNT diameter and E_{laser}, while the dependence of ω_{RBM} on the chiral angle θ is rather weak, even for SWNTs with $d_t < 1$ nm, where the dependence of ω_{RBM} reaches a few wave numbers.

(iii) For a given SWNT, the RBM peak intensity I (E_{laser}) is a function of E_{laser} due to resonance effects with the one-dimensional van Hove singularities. The RBM is intense when the incident light (E_{laser}) or the scattered light $(E_{laser} \pm \omega_{RBM})$ is in resonance with the SWNT optical transition energies E_{ii}.

(iv) The optical transition energies E_{ii} can be obtained using resonance Raman spectroscopy. The theoretical description depends on an accurate analysis of the nanotube structure, exciton effects, and dielectric screening.

(v) The electron-photon and electron-phonon matrix elements for the RBM intensity, as well as the resonance broadening factor γ_r, strongly depend on (n, m).

(vi) The RBM is a totally symmetric mode. The polarization dependence is dominated by the antenna effect, where a strong Raman signal is observed when both the incident and scattered lights are chosen along the tube axis.

(vii) The same inner (n, m) tube within a double wall-carbon nanotube (DWNT) can exhibit different ω_{RBM} values if surrounded by different outer (n', m') tubes.

(viii) Usually in the RBM, linewidth is in the range of 3 cm^{-1}, although it can reach much larger values (by one order of magnitude) due to environmental effects, or smaller (also by as much as one order of magnitude) when measured for the inner tube of a DWNT and at low temperature.

(ix) Due to the relatively low RBM frequency, changes in ω_{RBM} with temperature, doping, strain, and other such effects are less pronounced in the RBM than in the ω_G from the G band. However, the RBM becomes important when looking for the effects on one single (n, m) specie among many SWNTs, since the RBM feature is unique for each (n, m) (ω_{RBM} depends strongly on tube diameter), while the G band appears within the same frequency range for most SWNTs (weak d_t dependence).

(x) As discussed above, changes in temperature, pressure or the dielectric constant of the environment do not change ω_{RBM} significantly. However, these factors do change E_{ii}, and changing the resonance condition changes the RBM intensity. Therefore, the RBM can be used to probe resonance effects sensitively, and for understanding the importance of excitonic effects for a theoretical description of the observed Raman spectra. Increasing the temperature decreases E_{ii}, and the temperature-dependent change in E_{ii} also depends on (n, m). Increasing the pressure changes E_{ii}, and the pressure-dependent changes in E_{ii} also depend on (n, m). Here a change in E_{ii} can be positive or negative, depending on i and on the mod($2n + m, 3$) type. Increasing the dielectric constant of an SWNT-wrapping agent decreases E_{ii}.

(xi) The Stokes versus anti-Stokes (S/aS) intensity ratio for the RBM features is strongly sensitive to the energy displacement of E_{laser} with respect to E_{ii}.

7. Pushing the Limits of Raman Spectroscopy Applications on sp^2 Nanocarbons

The state-of-the-art experiments are pushing the limits of Raman spectroscopy and its applications to carbon nanoscience.

The ability to perform nanomanipulation and Raman spectroscopy is important for a well-controlled study of intrinsic and extrinsic properties of nanostructures. Superlattice graphene structures can be generated in bilayer graphene, by inducing a mismatch angle θ between the top and bottom layers [62–66] (see the left part of Figure 6). Such graphene superlattices can be formed by nanomanipulation, for example, by folding graphene into itself with an atomic force microscopy (AFM) tip [67].
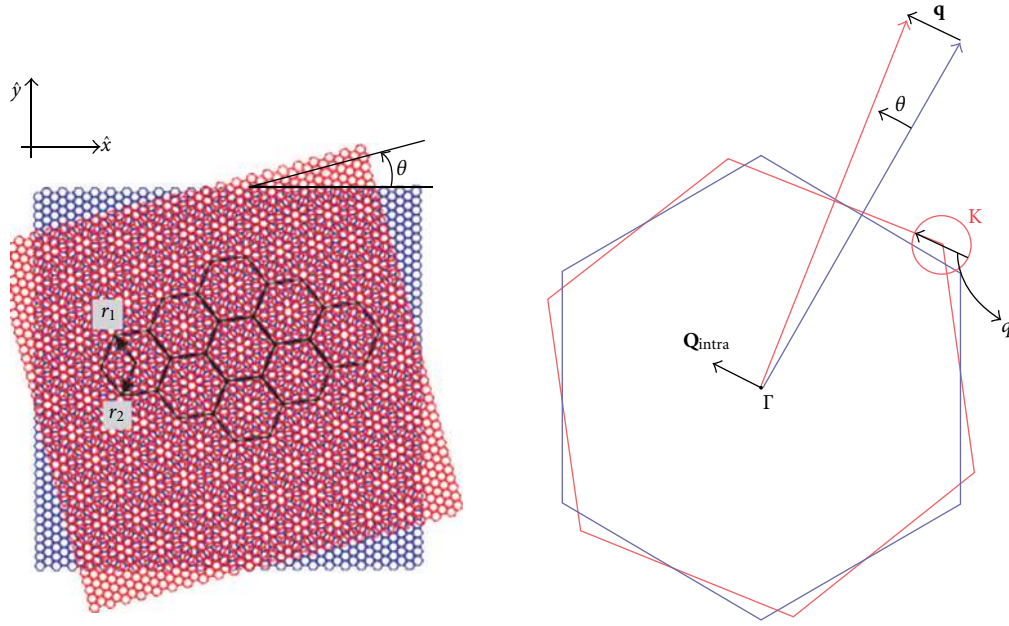
FIGURE 6: The formation of graphene superstructures by rotating the two layers of bilayer graphene, one with respect to the other. The mismatch angle θ defines the superstructure (left), which is characterized in the momentum space by a modulation $\mathbf{q}$ vector (right).

The superlattice formation was recently shown to activate new Raman modes from the interior of the graphene phonon Brillouin zone [67–70], as a new type of multiple-resonance phenomena in sp^2 nanocarbons. Different from what was discussed in Section 5, here the modulation in the superlattice, which is characterized by a momentum $\mathbf{Q}_{intra}(\theta) = \mathbf{q}(\theta)$ (see right part of Figure 6), will generate the momentum required for momentum conservation in the multiple-resonance scattering mechanism [67]. Alternatively one could say that in the superstructure, the interior of the Brillouin zone is folded into the Γ point, which is equivalent. Specific θ generates specific Raman frequencies that will appear resonantly in the Raman spectra when the right E_{laser} is used. These new features have been called R' (from "rotation") when related to a double-resonance intra-valley process ($\mathbf{Q}_{intra}$, like in Figure 6), appearing above the G band frequency, and R when related to a double-resonance inter-valley process ($\mathbf{Q}_{inter}$, not shown here), appearing below the G band frequency [67].

Furthermore, the G band intensity in graphene super-lattices was shown to exhibit a large intensity enhancement for specific combined values of θ and excitation laser energy E_{laser} [71–73]. This effect happens due to resonance achieved with the new van Hove singularity (vHS) that appears in the electronic joint density of states due to the superstructure formation. In this case, the unusual enhancement is not due to multiple-resonance effects, but rather due to achieving resonance with a specific energy where the density of electronic states is unusually large (the vHS). This new result shows that Raman spectroscopy can probe the changes in the electronic structure due to the superlattice formation.

Another example of recent experiments where nanomanipulation has been combined with Raman spectroscopy was developed in carbon nanotubes. Raman spectroscopy has been broadly used to study effects caused by strain, majorly focusing on the G band behaviour on SWNT bundles [74–80]. Combination of AFM with confocal Raman spectroscopy was made to follow, *in situ*, the evolution of the SWNT structure with transversal pressure applied to the tube. The G band feature in isolated SWNTs deposited on a substrate was monitored while pressing the tube with the AFM tip [81].

The G band, which is related to two phonon branches degenerated at the Γ point (see phonon dispersion in Figure 3), splits in SWNTs due to the tube curvature (see G$^+$ and G$^-$ in Figure 5). In achiral SWNTs, the G band splits into LO and TO modes, where longitudinal and transversal here stand for parallel and perpendicular to the tube axis. The experiments performed on isolated SWNTs [81] evidenced a previously elusive and fundamental symmetry-breaking effect for the totally symmetric TO G-band mode, which exhibited two distinct Raman-active features with increasing applied pressure. One of the features is related to atomic motion localized at the flattened regions, while the other feature is related to atomic motion localized at the curved regions of the ovalized SWNT.

However, different SWNTs showed different G$^+$ and G$^-$ band behaviours. For example, in one case, rather than the TO (G$^-$) splitting discussed in the previous paragraph, the observed effect was the increase in the splitting between the G$^+$ and G$^-$ modes in SWNTs, indicating in that case that the LO versus TO nature was not identified. This result is expected for chiral SWNTs, where the C–C bonds exhibit a helical structure, and the LO versus TO nature for the two G band peaks is indeed not expected. These results showed the richness of transversal deformation at the isolated

SWNT level [81], which are averaged out on SWNT bundle measurements.

Besides the ability to perform nanomanipulation and Raman spectroscopy experiments to perform detailed studies, another advance is the multitechnique approach, which is important for the development of nanometrology. Generally speaking, for the development of accurate Raman-based analysis, systematic calibration procedures are necessary. One way is making use of a microscopy technique to independently quantify any specific effect that will be further probed with Raman spectroscopy.

Combined Raman spectroscopy, ion bombardment, and scanning tunnelling microscopy (STM) were applied to study the evolution of peak frequencies, intensities, linewidths, and integrated areas of the main Raman bands of graphene, as a function of ion bombardment dose [82, 83]. The main effects are displayed in Figure 7. On the left side of Figure 7, one sees three STM images of the sp^2 carbon surfaces before ion bombardment (pristine), after 10^{11} Ar^+/cm^2 ion dose, and after 10^{14} Ar^+/cm^2. Point defects appear for the low ion dose, and amorphization of the graphene surface takes place for the larger ion dose. On the right side of Figure 7, the respective Raman spectra for the graphene samples at the same ion bombardment levels are shown. For pristine graphene, only the G band is observed. For defective graphene, the D and D′ peaks appear. Large bombardment ion dose generates high level of disorder, and the respective Raman spectrum becomes typical of amorphous carbon, marked by broad bands (compare with the bottom spectrum in Figure 5).

Systematic work was developed for calibrating the intensity ratio between the D and G peaks (I_D/I_G) in graphene as a function of ion dose, and this is reported in [82, 83]. The Raman relaxation length for the disorder-induced Raman scattering process in graphene was also established in these experiments, and 2 nm [82] was found, a value that is at least 10 times more accurate than the values previously published in the literature [84, 85]. This work was extended to study the effect of low-energy (90 eV) Ar^+ ion bombardment in graphene samples as a function of the number of layers [86, 87]. In sequence, the I_D/I_G dependence on the excitation laser energy E_{laser}, already established for nanographite [88, 89], was extended to point defects in graphene [90], thus providing a formula for quantifying the amount of defects in graphene for any excitation laser energy.

The multitechnique approach has also been used in the development of nanometrology on single-wall carbon nanotubes (SWNTs). The Raman spectra from the radial breathing modes (RBMs) have been largely used to give information about the diameter distribution in the samples [2, 9]. However, it is known that the Raman cross-section itself depends strongly on the tube diameter, mostly due to the diameter dependence on the excitonic effects [57]. Pesce et al. [91] used a high-resolution transmission electron microscopy (HRTEM) protocol to measure the SWNT diameter distribution in a bundles sample and compared the results with the RBM resonance Raman map. This procedure was used to calibrate the diameter dependence of the RBM Raman cross-section, thus establishing a method for accurate determination of the diameter distribution in an SWNT sample using Raman spectroscopy [91].

As can be seen here, the nanoscience and nanometrology of Raman spectroscopy applied to sp^2 nanocarbons are maturing. Consequently, the Raman spectroscopy is now being applied to develop cross-related fields. Basically, wherever sp^2 carbon nanostructures are used, the Raman scattering can help detecting and characterizing. Spectral imaging can be used to detect and locate the sp^2 nanocarbons inside biological materials, for example, while Raman frequency shifts indicate and quantify carbon-environment interactions.

One example of application in biotechnology: different studies have evaluated the ability of SWNTs and multiwall carbon nanotubes (MWNTs) as transfection agents to deliver gene materials [92–95]. Ladeira et al. [96] demonstrated highly efficient RNA delivery system into human and murine cells using MWNTs. They applied a G band MWNT confocal imaging to demonstrate the presence of MWNTs inside neonatal cardiomyocytes, confirming the ability of MWNTs to enter this cell.

Another example is the study of soil sciences: the carbon materials found in specific sites in the Amazonian forest, where Indians subsisted on agriculture in addition to hunting, fishing, and gathering activities [97]. Their way of life generated areas of highly fertile soils, rich in plant nutrients, known as "*Terra Preta de Índio*" (Amazonian Dark Earth) [98–103]. This phenomenon is more frequent in the Amazon, but it can also be found in other regions of South America and Africa [104, 105]. The soil recalcitrance is known to be due to a large amount of stable carbons in these soils, which are responsible for their black colour.

In sp^2 nanocarbons, Raman spectroscopy has been used to measure the nanocrystallite graphite dimensions, which are defined by the in-plane crystallite size (L_a) [11, 88, 89, 106, 107]. One way of doing it is to correlate the G band linewidth with L_a, as accurately developed by Cançado et al. [88, 89]. This protocol was used to elucidate the nanostructure of the stable carbon materials found in the "*Terra Preta do Índio*," which were shown to be majorly sp^2 nanocarbons [108]. The results were then compared with results obtained in charcoal samples, which are being used in attempts to reproduce the "*Terra Preta do Índio*" soil. Under the Raman spectroscopy analysis, the crystallite size distribution was found to be in the 3–8 nm range in the "*Terra Preta do Índio*" sp^2 nanocarbons, while in commonly produced charcoal, it was found as typically between 8 and 12 nm. This provides imputes from nanotechnology, based on Raman spectroscopy [108], for the development of new routes to generate a nanocarbon structure that would be suitable for the generation of stable and highly productive soils in the humid tropics, similar to the "*Terra Preta do Índio*."

8. Conclusion

In conclusion, Raman spectroscopy is already established as a powerful tool to characterize the different types of sp^2 carbon nanostructures, for the development of nanoscience and
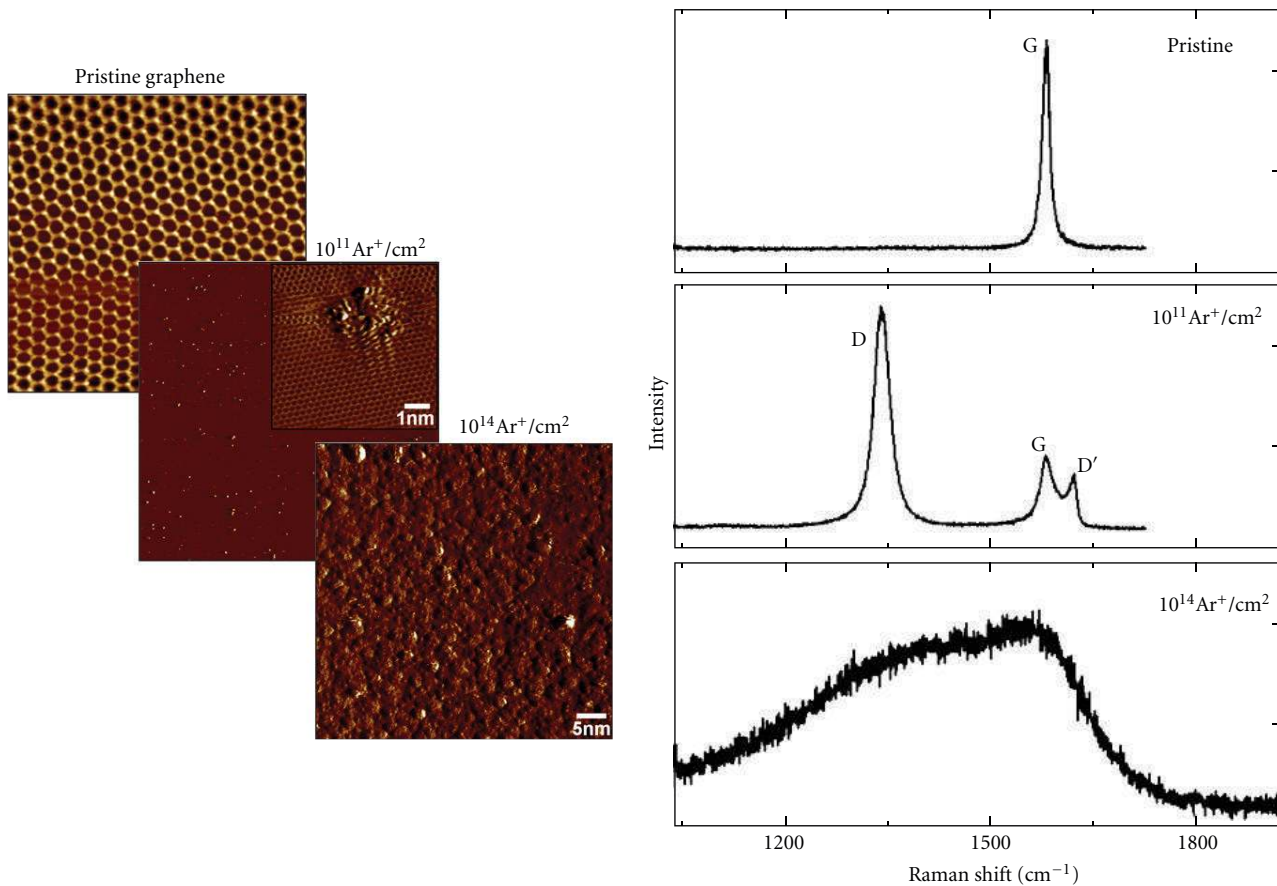
FIGURE 7: Scanning tunneling microscopy (left) and Raman spectroscopy (right) to characterize Ar$^+$ bombardment in graphene [82]. The ion doses are written near each STM image and Raman spectrum. The graphene G band and the disorder-induced D and D$'$ bands are indicated in the Raman spectra.

nanometrology. Here, the rather rich Raman spectra of sp^2 nanocarbons, composed by many peaks induced by single- and multiple-resonance effects, were discussed in depth. The properties of the main Raman peaks were described, including their dependence on both materials structure and external factors, like temperature, pressure, doping, and the environment.

This knowledge can be used as a guide for the use of Raman spectroscopy to characterize sp^2 nanocarbons, and recent applications are already pushing the limits of the technique, in graphene superlattices, for example, but also connecting Raman spectroscopy to other fields where the sp^2 nanocarbons are being utilized, like biotechnology and soil science.

Furthermore, the study of new materials is always a challenge that promises important new findings. New carbon nanostructures, like nanocones, which hold strong promises of several interesting mechanical, thermal, and electronic properties, have been addressed mostly theoretically [109–112]. Carbon nanocones are likely to find in Raman spectroscopy a key development technique starting point. Another route is using the knowledge on graphene to study other few layer materials, like MoS$_2$ and BN [113–115].

Raman spectroscopy is likely to play an important role in such explorations as well.

A challenge for a big step forward on the potential of Raman spectroscopy for developing even further nanoscience and nanometrology lies in the tip-enhanced Raman spectroscopy (TERS) technique. However, the high resolution (∼10 nm) instrumental setups are still at the home-built development stage, and severe instrumental work is still needed for achieving reliable results. The main challenge for TERS is the development of new and robust instrumentation for achieving a ready-to-use system. TERS in sp^2 nanocarbons started focusing on experimental work [23–30], but recently theoretical studies are appearing in both one-dimensional (SWNTs) [116] and two-dimensional (graphene) [117] materials, thus guiding the way for future developments.
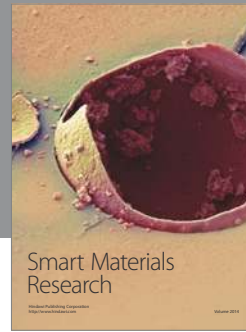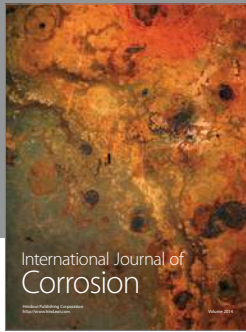
Acknowledgments

References

[1] V. Raman, *The Molecular Scattering of Light*, Nobel Lecture, 1930.

[2] A. Jorio, M. S. Dresselhaus, R. Saito, and G. Dresselhaus, *Raman Spectroscopy in Graphene Related Systems*, Wiley-VCH, Weinheim, Germany, 2011.

[3] F. Tuinstra and J. L. Koenig, "Raman spectrum of graphite," *Journal of Chemical Physics*, vol. 53, no. 3, pp. 1126–1130, 1970.

[4] R. Vidano and D. B. Fischbach, "New lines in the Raman spectra of carbons and graphite," *Journal of the American Ceramic Society*, vol. 61, no. 1-2, pp. 13–17, 1978.

[5] R. J. Nemanich and S. A. Solim, "First- and second-order Raman scattering from finite-size crystals of graphite," *Physical Review B*, vol. 20, pp. 392–401, 1979.

[6] M. S. Dresselhaus and R. Kalish, *Ion Implantation in Diamond Graphite and Related Materials*, Materials Science, Springer, Berlin, Germany, 1992.

[7] M. S. Dresselhaus, G. Dresselhaus, and P. C. Eklund, *Science of Fullerenes and Carbon Nanotubes*, Academic, New York, NY, USA, 1996.

[8] A. Jorio, R. Saito, G. Dresselhaus, and M. S. Dresselhaus, "Determination of nanotubes properties by Raman spectroscopy," *Philosophical Transactions of the Royal Society A*, vol. 362, no. 1824, pp. 2311–2336, 2004.

[9] R. Saito, M. Hofmann, G. Dresselhaus, A. Jorio, and M. S. Dresselhaus, "Raman spectroscopy of graphene and carbon nanotubes," *Advances in Physics*, vol. 60, no. 3, pp. 413–550, 2011.

[10] C. Castiglioni, M. Tommasini, and G. Zerbi, *Philosophical Transactions of the Royal Society of London*, vol. 362, pp. 2425–2459, 2004.

[11] A. C. Ferrari and J. Robertson, "Interpretation of Raman spectra of disordered and amorphous carbon," *Physical Review B*, vol. 61, pp. 14095–14107, 2000.

[12] C. Thomsen and S. Reich, "Double resonant Raman scattering in graphite," *Physical Review Letters*, vol. 85, pp. 5214–5217, 2000.

[13] R. Saito, A. Jorio, A. G. Souza Filho, G. Dresselhaus, M. S. Dresselhaus, and M. A. Pimenta, "Probing phonon dispersion relations of graphite by double resonance Raman scattering," *Physical Review Letters*, vol. 88, Article ID 027401, 4 pages, 2002.

[14] A. M. Rao, A. Jorio, M. A. Pimenta et al., "Polarized Raman study of aligned multiwalled carbon nanotubes," *Physical Review Letters*, vol. 84, no. 8, pp. 1820–1823, 2000.

[15] A. Jorio, G. Dresselhaus, M. S. Dresselhaus et al., "Polarized Raman study of single-wall semiconducting carbon nanotubes," *Physical Review Letters*, vol. 85, no. 12, pp. 2617–2620, 2000.

[16] A. Jorio, M. A. Pimenta, A. G. Sousa Filho et al., "Resonance Raman spectra of carbon nanotubes by cross-polarized light," *Physical Review Letters*, vol. 90, no. 10, p. 107403, 2003.

[17] E. B. Barros, A. Jorio, G. G. Samsonidze et al., "Review on the symmetry-related properties of carbon nanotubes," *Physics Reports*, vol. 431, no. 6, pp. 261–302, 2006.

[18] A. Jorio, R. Saito, J. H. Hafner et al., "Structural (n, m) determination of isolated single-wall carbon nanotubes by resonant Raman scattering," *Physical Review Letters*, vol. 86, no. 6, pp. 1118–1121, 2001.

[19] L. G. Cançado, M. A. Pimenta, B. R. A. Neves et al., "Anisotropy of the Raman spectra of nanographite ribbons," *Physical Review Letters*, vol. 93, no. 4, Article ID 047403, 1 pages, 2004.

[20] A. G. Souza Filho, A. Jorio, A. K. Swan et al., "Anomalous two-peak G′-band Raman effect in one isolated single-wall carbon nanotube," *Physical Review B*, vol. 65, pp. 085417–085424, 2002.

[21] A. C. Ferrari, J. C. Meyer, V. Scardaci et al., "Raman spectrum of graphene and graphene layers," *Physical Review Letters*, vol. 97, no. 18, Article ID 187401, 2006.

[22] A. Gupta, G. Chen, P. Joshi, S. Tadigadapa, and P. C. Eklund, "Raman scattering from high-frequency phonons in supported n-graphene layer films," *Nano Letters*, vol. 6, no. 12, pp. 2667–2673, 2006.

[23] A. Hartschuh, E. J. Sánchez, X. S. Xie, and L. Novotny, "High-resolution near-field Raman microscopy of single-walled carbon nanotubes," *Physical Review Letters*, vol. 90, Article ID 95503, 4 pages, 2003.

[24] N. Hayazawa, T. Yano, H. Watanabe, Y. Inouye, and S. Kawata, "Detection of an individual single-wall carbon nanotube by tip-enhanced near-field Raman spectroscopy," *Chemical Physics Letters*, vol. 376, no. 1-2, pp. 174–180, 2003.

[25] N. Anderson, A. Hartschuh, S. Cronin, and L. Novotny, "Nanoscale vibrational analysis of single-walled carbon nanotubes," *Journal of the American Chemical Society*, vol. 127, no. 8, pp. 2533–2537, 2005.

[26] A. Hartschuh, H. Qian, A. J. Meixner, N. Anderson, and L. Novotny, "Nanoscale optical imaging of excitons in single-walled carbon nanotubes," *Nano Letters*, vol. 5, no. 11, pp. 2310–2313, 2005.

[27] Y. Saito, N. Hayazawa, H. Kataura et al., "Polarization measurements in tip-enhanced Raman spectroscopy applied to single-walled carbon nanotubes," *Chemical Physics Letters*, vol. 410, no. 1–3, pp. 136–141, 2005.

[28] N. Anderson, A. Hartschuh, and L. Novotny, "Chirality changes in carbon nanotubes studied with near-field Raman spectroscopy," *Nano Letters*, vol. 7, no. 3, pp. 577–582, 2007.

[29] I. O. Maciel, N. Anderson, M. A. Pimenta et al., "Electron and phonon renormalization near charged defects in carbon nanotubes," *Nature Materials*, vol. 7, no. 11, pp. 878–883, 2008.

[30] H. Qian, P. T. Araujo, C. Georgi et al., "Visualizing the local optical response of semiconducting carbon nanotubes to DNA-wrapping," *Nano Letters*, vol. 8, no. 9, pp. 2706–2711, 2008.

[31] L. G. Cançado, A. Hartschuh, and L. Novotny, "Tip-enhanced Raman spectroscopy of carbon nanotubes," *Journal of Raman Spectroscopy*, vol. 40, no. 10, pp. 1420–1426, 2009.

[32] G. G. Hoffmann, G. de With, and J. Loos, "Micro-Raman and tip-enhanced Raman spectroscopy of carbon allotropes," *Macromolecular Symposia*, vol. 265, no. 1, pp. 1–11, 2008.

[33] Y. Saito, P. Verma, K. Masui, Y. Inouye, and S. Kawata, "Nano-scale analysis of graphene layers by tip-enhanced near-field Raman spectroscopy," *Journal of Raman Spectroscopy*, vol. 40, no. 10, pp. 1434–1440, 2009.

[34] K. F. Domke and B. Pettinger, "Tip-enhanced Raman spectroscopy of 6H-SiC with graphene adlayers: selective suppression of E1 modes," *Journal of Raman Spectroscopy*, vol. 40, no. 10, pp. 1427–1433, 2009.

[35] V. Snitka, R. D. Rodrigues, and V. Lendraitis, "Novel gold cantilever for nano-Raman spectroscopy of graphene," *Microelectronic Engineering*, vol. 88, no. 8, pp. 2759–2762, 2011.

[36] J. Stadler, T. Schmid, and R. Zenobi, "Nanoscale chemical imaging of single-layer graphene," *ACS Nano*, vol. 5, pp. 8442–8448, 2011.

[37] L. G. Cançado, M. A. Pimenta, B. R. A. Neves, M. S. S. Dantas, and A. Jorio, "Influence of the atomic structure on the Raman spectra of graphite edges," *Physical Review Letters*, vol. 93, Article ID 247401, 2004.

[38] C. Casiraghi, A. Hartschuh, H. Qian et al., "Raman spectroscopy of graphene edges," *Nano Letters*, vol. 9, no. 4, pp. 1433–1441, 2009.

[39] M. Tommasini, C. Castiglioni, and G. Zerbi, "Raman scattering of molecular graphenes," *Physical Chemistry Chemical Physics*, vol. 11, no. 43, pp. 10185–10194, 2009.

[40] A. G. S. Filho, A. Jorio, G. G. Samsonidze, G. Dresselhaus, R. Saito, and M. S. Dresselhaus, "Raman spectroscopy for probing chemically/physically induced phenomena in carbon nanotubes," *Nanotechnology*, vol. 14, no. 10, pp. 1130–1139, 2003.

[41] P. Corio, A. Jorio, N. Demir, and M. S. Dresselhaus, "Spectroelectrochemical studies of single wall carbon nanotubes films," *Chemical Physics Letters*, vol. 392, no. 4–6, pp. 396–402, 2004.

[42] A. Jorio, A. G. Souza Filho, G. Dresselhaus et al., "G-band resonant Raman study of 62 isolated single-wall carbon nanotubes," *Physical Review B*, vol. 65, p. 155412, 2002.

[43] A. G. Souza Filho, A. Jorio, G. Dresselhaus et al., "Effect of quantized electronic states on the dispersive Raman features in individual single-wall carbon nanotubes," *Physical Review B*, vol. 65, Article ID 035404, 6 pages, 2001.

[44] S. Piscanec, M. Lazzeri, F. Mauri, A. C. Ferrari, and J. Robertson, "Kohn anomalies and electron-phonon interactions in graphite," *Physical Review Letters*, vol. 93, no. 18, Article ID 185503, 4 pages, 2004.

[45] A. Das, S. Pisana, B. Chakraborty et al., "Monitoring dopants by Raman scattering in an electrochemically top-gated graphene transistor," *Nature Nanotechnology*, vol. 3, no. 4, pp. 210–215, 2008.

[46] M. Kalbac, L. Kavan, L. Dunsch, and M. S. Dresselhaus, "Development of the tangential mode in the Raman spectra of SWCNT bundles during electrochemical charging," *Nano Letters*, vol. 8, no. 4, pp. 1257–1264, 2008.

[47] J. S. Park, K. Sasaki, R. Saito et al., "Fermi energy dependence of the G -band resonance Raman spectra of single-wall carbon nanotubes," *Physical Review B*, vol. 80, no. 8, Article ID 081402, 2009.

[48] S. Piscanec, M. Lazzeri, J. Robertson, A. C. Ferrari, and F. Mauri, "Optical phonons in carbon nanotubes: Kohn anomalies, Peierls distortions, and dynamic effects," *Physical Review B*, vol. 75, Article ID 035427, 22 pages, 2007.

[49] T. M. G. Mohiuddin, A. Lombardo, R. R. Nair et al., "Uniaxial strain in graphene by Raman spectroscopy: G peak splitting, Grüneisen parameters, and sample orientation," *Physical Review B*, vol. 79, no. 20, Article ID 205433, 8 pages, 2009.

[50] E. Di Donato, M. Tommasini, C. Castiglioni, and G. Zerbi, "Assignment of the G^+ and G^- Raman bands of metallic and semiconducting carbon nanotubes based on a common valence force field," *Physical Review B*, vol. 74, Article ID 184306, 12 pages, 2006.

[51] C. Fantini, A. Jorio, M. Souza, M. S. Strano, M. S. Dresselhaus, and M. A. Pimenta, "Optical transition energies for carbon nanotubes from resonant Raman spectroscopy: environment and temperature effects," *Physical Review Letters*, vol. 93, no. 14, Article ID 147406, 4 pages, 2004.

[52] H. Telg, J. Maultzsch, S. Reich, F. Hennrich, and C. Thomsen, "Chirality distribution and transition energies of carbon nanotubes," *Physical Review Letters*, vol. 93, no. 17, Article ID 177401, 4 pages, 2004.

[53] P. T. Araujo, S. K. Doorn, S. Kilina et al., "Third and fourth optical transitions in semiconducting carbon nanotubes," *Physical Review Letters*, vol. 98, no. 6, Article ID 067401, 4 pages, 2007.

[54] S. K. Doorn, P. T. Araujo, K. Hata, and A. Jorio, "Excitons and exciton-phonon coupling in metallic single-walled carbon nanotubes: resonance Raman spectroscopy," *Physical Review B*, vol. 78, Article ID 165408, 9 pages, 2008.

[55] R. Pfeiffer, F. Simon, H. Kuzmany, and V. N. Popov, "Fine structure of the radial breathing mode of double-wall carbon nanotubes," *Physical Review B*, vol. 72, no. 16, pp. 1–4, 2005.

[56] J. Jiang, R. Saito, A. Grüneis et al., "Photoexcited electron relaxation processes in single-wall carbon nanotubes," *Physical Review B*, vol. 71, no. 4, Article ID 045417, 9 pages, 2005.

[57] J. Jiang, R. Saito, K. Sato et al., "Exciton-photon, exciton-phonon matrix elements, and resonant Raman intensity of single-wall carbon nanotubes," *Physical Review B*, vol. 75, no. 3, Article ID 035405, 2007.

[58] P. T. Araujo, I. O. Maciel, P. B. C. Pesce et al., "Nature of the constant factor in the relation between radial breathing mode frequency and tube diameter for single-wall carbon nanotubes," *Physical Review B*, vol. 77, no. 24, Article ID 241403, 2008.

[59] P. T. Araujo, A. Jorio, M. S. Dresselhaus, K. Sato, and R. Saito, "Diameter dependence of the dielectric constant for the excitonic transition energy of single-wall carbon nanotubes," *Physical Review Letters*, vol. 103, Article ID 146802, 4 pages, 2009.

[60] A. R. T. Nugraha, R. Saito, K. Sato, P. T. Araujo, A. Jorio, and M. S. Dresselhaus, "Dielectric constant model for environmental effects on the exciton energies of single wall carbon nanotubes," *Applied Physics Letters*, vol. 97, Article ID 091905, 3 pages, 2010.

[61] P. H. Tan, C. Y. Hu, J. Dong, W. C. Shen, and B. F. Zhang, "Polarization properties, high-order Raman spectra, and frequency asymmetry between Stokes and anti-Stokes scattering," *Physical Review B*, vol. 64, Article ID 214301, 12 pages, 2001.

[62] E. J. Mele, "Commensuration and interlayer coherence in twisted bilayer graphene," *Physical Review B*, vol. 81, Article ID 161405, 4 pages, 2010.

[63] G. Li, A. Luican, J. M. B. Lopes Dos Santos et al., "Observation of Van Hove singularities in twisted graphene layers," *Nature Physics*, vol. 6, no. 2, pp. 109–113, 2010.

[64] W. Kohn and J. M. Luttinger, "New mechanism for superconductivity," *Physical Review Letters*, vol. 15, no. 12, pp. 524–526, 1965.

[65] T. M. Rice and G. K. Scott, "New Mechanism for a charge-density-wave instability," *Physical Review Letters*, vol. 35, pp. 120–123, 1975.

[66] M. Fleck, A. M. Oleś, and L. Hedin, "Magnetic phases near the Van Hove singularity in s- and d-band Hubbard models," *Physical Review B*, vol. 56, pp. 3159–3166, 1997.

[67] V. Carozo, C. M. Almeida, E. H. M. Ferreira, L. G. Cançado, C. A. Achete, and A. Jorio, "Raman signature of graphene superlattices," *Nano Letters*, vol. 11, pp. 4527–4534, 2011.

[68] A. K. Gupta, Y. Tang, V. H. Crespi, and P. C. Eklund, "Nondispersive Raman D band activated by well-ordered interlayer interactions in rotationally stacked bilayer graphene," *Physical Review B*, vol. 82, Article ID 241406, 4 pages, 2010.

[69] A. Righi, S. D. Costa, H. Chacham et al., "Graphene Moiré patterns observed by umklapp double-resonance Raman scattering," *Physical Review B*, vol. 84, Article ID 241409, 4 pages, 2011.

[70] R. Podila, R. Rao, R. Tsuchikawa, M. Ishigami, and A. M. Rao, "Raman spectroscopy of folded and scrolled graphene," *ACS Nano*, vol. 6, no. 7, pp. 5784–5790, 2012.

[71] Z. Ni, L. Liu, Y. Wang et al., "G -band Raman double resonance in twisted bilayer graphene: evidence of band splitting and folding," *Physical Review B*, vol. 80, no. 12, Article ID 125404, 5 pages, 2009.

[72] R. W. Havener, H. Zhuang, L. Brown, R. G. Hennig, and J. Park, "Angle-resolved Raman imaging of interlayer rotations and interactions in twisted bilayer graphene," *Nano Letters*, no. 12, pp. 3162–3167, 2012.

[73] K. Kim, S. Coh, L. Z. Tan et al., "Raman spectroscopy study of rotated double-layer graphene: misorientation-angle dependence of electronic structure," *Physical Review Letters*, vol. 108, pp. 246103–246108, 2012.

[74] S. Reich, C. Thomsen, and P. Ordejón, "Elastic properties of carbon nanotubes under hydrostatic pressure," *Physical Review B*, vol. 65, Article ID 153407, 4 pages, 2002.

[75] S. B. Cronin, A. K. Swan, M. S. Ünlü, B. B. Goldberg, M. S. Dresselhaus, and M. Tinkham, "Measuring the uniaxial strain of individual single-wall carbon nanotubes: resonance Raman spectra of atomic-force-microscope modified single-wall nanotubes," *Physical Review Letters*, vol. 93, pp. 167401–167405, 2004.

[76] B. Gao, L. Jiang, X. Ling, J. Zhang, and Z. Liu, "Chirality-dependent Raman frequency variation of single-walled carbon nanotubes under uniaxial strain," *Journal of Physical Chemistry C*, vol. 112, no. 51, pp. 20123–20125, 2008.

[77] A. G. S. Filho, N. Kobayashi, J. Jiang et al., "Strain-induced interference effects on the resonance Raman cross section of carbon nanotubes," *Physical Review Letters*, vol. 95, no. 21, Article ID 217403, 4 pages, 2005.

[78] X. Yang, G. Wu, and J. Dong, "Structural transformations of double-walled carbon nanotube bundle under hydrostatic pressure," *Applied Physics Letters*, vol. 89, pp. 113101–113103, 2006.

[79] M. Yao, Z. Wang, B. Liu et al., "Raman signature to identify the structural transition of single-wall carbon nanotubes under high pressure," *Physical Review B*, vol. 78, no. 20, Article ID 205411, 2008.

[80] A. L. Aguiar, E. B. Barros, R. B. Capaz et al., "Pressure-induced collapse in double-walled carbon nanotubes: chemical and mechanical screening effects," *Journal of Physical Chemistry C*, vol. 115, no. 13, pp. 5378–5384, 2011.

[81] P. T. Araujo, N. M. B. Neto, H. Chacham et al., "In situ atomic force microscopy Tip-induced deformations and Raman spectroscopy characterization of single-wall carbon nanotubes," *Nano Letters*, vol. 12, no. 8, pp. 4110–4116, 2012.

[82] M. M. Lucchese, F. Stavale, E. H. M. Ferreira et al., "Quantifying ion-induced defects and Raman relaxation length in graphene," *Carbon*, vol. 48, no. 5, pp. 1592–1597, 2010.

[83] E. H. M. Ferreira, M. V. O. Moutinho, F. Stavale et al., "Evolution of the Raman spectra from single-, few-, and many-layer graphene with increasing disorder," *Physical Review B*, vol. 82, no. 12, Article ID 125429, 2010.

[84] L. G. Cançado, R. Beams, and L. Novotny, "Optical measurement of the phase-breakinglength in graphene," http://arxiv.org/abs/0802.3709.

[85] A. K. Gupta, T. J. Russin, H. R. Gutiérrez, and P. C. Eklund, "Probing graphene edges via Raman scattering," *ACS Nano*, vol. 3, no. 1, pp. 45–52, 2009.

[86] A. Jorio, M. M. Lucchese, F. Stavale et al., "Raman study of ion-induced defects in N -layer graphene," *Journal of Physics Condensed Matter*, vol. 22, no. 33, Article ID 334204, 2010.

[87] A. Jorio, M. M. Lucchese, F. Stavale, and C. A. Achete, "Raman spectroscopy study of Ar+ bombardment in highly oriented pyrolytic graphite," *Physica Status Solidi B*, vol. 246, no. 11-12, pp. 2689–2692, 2009.

[88] L. G. Cançado, K. Takai, T. Enoki et al., "General equation for the determination of the crystallite size L_a of nanographite by Raman spectroscopy," *Applied Physics Letters*, vol. 88, Article ID 163106, 3 pages, 2006.

[89] L. G. Cançado, A. Jorio, and M. A. Pimenta, "Measuring the absolute Raman cross section of nanographites as a function of laser energy and crystallite size," *Physical Review B*, vol. 76, pp. 064304–064310, 2007.

[90] L. G. Cançado, A. Jorio, E. H. M. Ferreira et al., "Quantifying defects in graphene via Raman spectroscopy at different excitation energies," *Nano Letters*, vol. 11, no. 8, pp. 3190–3196, 2011.

[91] P. B. C. Pesce, P. T. Araujo, P. Nikolaev et al., "Calibrating the single-wall carbon nanotube resonance Raman intensity by high resolution transmission electron microscopy for a spectroscopy-based diameter distribution determination," *Applied Physics Letters*, vol. 96, Article ID 051910, 3 pages, 2010.

[92] N. W. Kam, Z. Liu, and H. Dai, "Functionalization of carbon nanotubes via cleavable disulfide bonds for efficient intracellular delivery of siRNA and potent gene silencing," *Journal of the American Chemical Society*, vol. 127, no. 36, pp. 12492–12493, 2005.

[93] K. Rege, G. Viswanathan, G. Zhu, A. Vijayaraghavan, P. M. Ajayan, and J. S. Dordick, "In vitro transcription and protein translation from carbon nanotube-DNA assemblies," *Small*, vol. 2, no. 6, pp. 718–722, 2006.

[94] Z. Zhang, X. Yang, Y. Zhang et al., "Delivery of telomerase reverse transcriptase small interfering RNA in complex with positively charged single-walled carbon nanotubes suppresses tumor growth," *Clinical Cancer Research*, vol. 12, pp. 4933–4939, 2006.

[95] R. Krajcik, A. Jung, A. Hirsch, W. Neuhuber, and O. Zolk, "Functionalization of carbon nanotubes enables noncovalent binding and intracellular delivery of small interfering RNA for efficient knock-down of genes," *Biochemical and Biophysical Research Communications*, vol. 369, no. 2, pp. 595–602, 2008.

[96] M. S. Ladeira, V. A. Andrade, E. R. M. Gomes et al., "Highly efficient siRNA delivery system into human and murine cells using single-wall carbon nanotubes," *Nanotechnology*, vol. 21, no. 38, Article ID 385101, 2010.

[97] M. F. Simões, "A Pré-História da Bacia Amazônica: 85 Uma tentativa de reconstituição," in *Cultura IndígEna, Textos e Catálogo*, pp. 5–21, Semana do Índio, Museu Goeldi, Brazil, 1982.

[98] D. C. Kern, *Geoquímica e Pedogeoquímica em sítios Arqueológicos com terra preta na Floresta Nacional de Caxiuanã [Ph.D. thesis]*, Universidade Federal do Pará, Belém, Brazil, 1996.

[99] N. J. H. Smith, "Anthrosols and human carrying capacity in amazonia," *Annals of the Association of American Geographers*, vol. 70, no. 4, pp. 553–566, 1980.

[100] N. P. S. Falcão, N. Comerford, and J. Lehmann, "Determining nutrient bioavailability of amazonian dark earth soils—methodological challenges," in *Amazonian Dark Earths, Origins, Properties, Management*, J. Lehmann, D. C. Kern, B. Glaser, and W. I. Woods, Eds., pp. 255–270, Kluwer Academic Publishers, 2003.

[101] B. Glaser, J. Lehmann, and W. Zech, "Ameliorating physical and chemical properties of highly weathered soils in the tropics with charcoal—a review," *Biology and Fertility of Soils*, vol. 35, no. 4, pp. 219–230, 2002.

[102] B. Glaser, "Prehistorically modified soils of central Amazonia: a model for sustainable agriculture in the twenty-first century," *Philosophical Transactions of the Royal Society A*, vol. 362, pp. 187–196, 2007.

[103] E. Marris, "Putting the carbon back: black is the new green," *Nature*, vol. 442, pp. 624–626, 2006.

[104] A. C. Blackmore, M. T. Mentis, and R. J. Scholes, "The origin and extent of nutrient-enriched patches within a nutrient-poor savanna in South Africa," *Journal of Biogeography*, vol. 17, no. 4-5, pp. 463–470, 1990.

[105] W. Zech, L. Haumaier, and R. Hempfling, "Ecological aspects of soil organic matter in tropical land use," in *Humic Substances in Soil and Crop Sciences: 15 Selected Readings.*, P. McCarthy, C. E. Clapp, R. L. Malcolm, and P. R. Bloom, Eds., pp. 187–202, American Society of Agronomy and Soil Science Society of America, Madison, Wis, USA, 1990.

[106] A. C. Ferrari and J. Robertson, "Resonant Raman spectroscopy of disordered, amorphous, and diamondlike carbon," *Physical Review B*, vol. 64, Article ID 075414, 13 pages, 2001.

[107] K. Takai, M. Oga, H. Sato et al., "Structure and electronic properties of a nongraphitic disordered carbon system and its heat-treatment effects," *Physical Review B*, vol. 67, no. 21, Article ID 214202, pp. 2142021–21420211, 2003.

[108] A. Jorio, J. Ribeiro-Soares, L. G. Cançado et al., "Microscopy and spectroscopy analysis of carbon nanostructures in highly fertile Amazonian anthrosoils," *Soil and Tillage Research*, vol. 122, pp. 61–66, 2012.

[109] J. C. Charlier and G. M. Rignanese, "Electronic structure of carbon nanocones," *Physical Review Letters*, vol. 86, no. 26 I, pp. 5970–5973, 2001.

[110] S. P. Jordan and V. H. Crespi, "Theory of carbon nanocones: mechanical chiral inversion of a micron-scale three-dimensional object," *Physical Review Letters*, vol. 93, Article ID 255504, 4 pages, 2004.

[111] N. Yang, G. Zhang, and B. Li, "Carbon nanocone: a promising thermal rectifier," *Applied Physics Letters*, vol. 93, Article ID 243111, 3 pages, 2008.

[112] M. Yudasaka, S. Iijima, and V. H. Crespi, "Single-wall carbon nanohorns and nanocones," *Topics in Applied Physics*, vol. 111, pp. 605–629, 2008.

[113] J. N. Coleman, M. Lotya, A. O'Neill et al., "Two-dimensional nanosheets produced by liquid exfoliation of layered materials," *Science*, vol. 331, no. 6017, pp. 568–571, 2011.

[114] B. Radisavljevic, A. Radenovic, J. Brivio, V. Giacometti, and A. Kis, "Single-layer MoS2 transistors," *Nature Nanotechnology*, vol. 6, no. 3, pp. 147–150, 2011.

[115] R. V. Gorbachev, I. Riaz, R. R. Nair et al., "Hunting for monolayer boron nitride: optical and Raman signatures," *Small*, vol. 7, no. 4, pp. 465–468, 2011.

[116] L. G. Cançado, A. Jorio, A. Ismach, E. Joselevich, A. Hartschuh, and L. Novotny, "Mechanism of near-field Raman enhancement in one-dimensional systems," *Physical Review Letters*, vol. 103, no. 18, Article ID 186101, 2009.

[117] R. V. Maximiano, R. Beams, L. Novotny, A. Jorio, and L. G. Cançado, "Mechanism of near-field Raman enhancement in two-dimensional systems," *Physical Review B*, vol. 85, Article ID 235434, 2012.